Self-consistent performance modeling for dualband detectors

S. G. Matsik[1] and A. G. U. Perera[2,a)]
[1]*NDP Optronics, LLC, Mableton, Georgia 30126, USA*
[2]*Department of Physics and Astronomy, Georgia State University, Atlanta, Georgia 30303, USA*

Dualband and multiband detectors have generated interest for their ability to measure two very different wavelength bands simultaneously. The dualband detection is achieved by using two different mechanisms to cover the two separate response bands: an interband process for the shorter wavelengths, and free carrier absorption followed by internal photoemission for the longer wavelengths. Previously the two processes have been modeled separately, and a reasonable agreement has been obtained on the spectral shape, although the entire wavelength range has not been covered in a single model. Also, the previous modeling efforts did not give an absolute scale for the response, instead using an experimentally determined gained factor to fix the absolute response. Here a model is presented (which does not use any fitting parameters) which can provide absolute responsivity values and detector performance parameters. By using a Monte Carlo approach including various scattering mechanisms, the carrier transport is modeled giving an absolute value for the dark current and photocurrent. The results are used to predict the spectral response for a GaN/AlGaN UV-IR dual band heterojunction detector. © *2008 American Institute of Physics*. [DOI: 10.1063/1.2967714]

I. INTRODUCTION

Multiband infrared detectors have seen increasing use in recent years.[1–5] Detectors covering a broad spectral range while at the same time having the ability to tailor and/or tune the spectral response range are in great demand. Dualband UV and IR detectors could find applications in fields such as fire fighting, where the ability to measure both UV and IR would help in identifying the nature of fires. These detectors would also be useful for space sensing as they would be solar blind, and hence unaffected by the sun. Optimized dualband detectors should show sensitivities similar to individual UV and IR detectors, making them ideal for such applications. Possible candidates for this role could be interfacial work-function internal photoemission (IWIP) detectors, which can be based on either homojunctions[6] (HIWIPs) or heterojunctions[7] (HEIWIPs) for which the spectral response models for free carrier response have been developed previously. These models use the absorption, photoemission, and collection efficiencies to calculate the response. The modeling for the absorption efficiency is readily calculated using a free carrier model, and the photoemission efficiency can be reasonably calculated using an escape cone[8,9] approach. However, the lack of a complete model which predicts the collection efficiency of the photoemitted carriers and any inherent gain of the detector has limited the predictive capabilities of the models. Hence, while it has been possible to predict the spectral shape of the response, the absolute value of the responsivity requires the knowledge of the gain factor. This can be estimated based on noise measurements assuming that the photocurrent and noise gains are the same. Typically the two gain factors agreed to within a factor of 2, but more accurate determinations require fitting the model spectra to the measured response,[10] and both methods do not give an *a priori* value for the gain.

This work is an effort to remedy this deficiency and at the same time to provide an approach that will allow the calculation of structures involving more complicated transitions, such as with both electrons and holes or from the light/ heavy to the split-off hole band.[11] The key feature of this approach is that it uses a Monte Carlo approach with the appropriate scattering rates (as discussed later) to determine both the probability of the carriers escaping from the emitters and the probability of the escaped carriers reaching the contacts and being collected. During this process, the model does not explicitly calculate the photoemission and collection efficiencies separately, but instead obtains the product of the two efficiencies. The combined escape and collection efficiencies will allow a direct determination of the absolute response of the detector.

An additional advantage of this model is that it can be readily extended to include additional absorption mechanisms, such as dealing with interband processes for which both electrons and holes are involved and also include impurity response. The model also obtains a self-consistent electric field distribution in the structure and, hence, can deal with both single emitter[12] and multi-emitter structures.[13] The limiting constraint on the number of layers in the structure will be the calculation time and the size of the matrices that can be handled.

The model will be tested by fitting results for a single barrier structure and using these to determine the optimum parameters for a single barrier dualband design. Although this is not the optimum design for a dualband detector, it provides a simple test structure for demonstrating the dualband effect. For a practical dualband design, a three contact structure with separate regions optimized for UV and IR re-

---

a)Also at NDP Optronics, LLC, GA 30126. Electronic mail: uperera@gsu.edu.
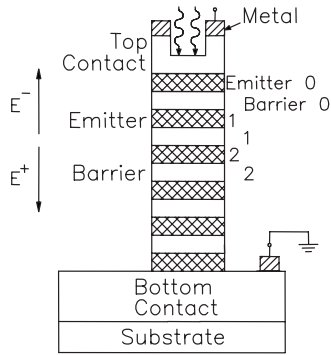
FIG. 1. The basic structure used for the model. The emitter layers are highly doped, while the barriers are not intentionally doped. The numbering of the emitters and barriers is shown on the right. The direction of propagation for the optical electric field is shown on the left.

sponses would be preferable. This would also prevent the UV response from being saturated by the 300 K background of the earth. The optimization of a multilayer structure would follow the same procedure except that the capture of carriers in the emitters would be more important for determining the gain.

II. BASIC MODEL FOR THE DETECTOR PERFORMANCE

The device modeling consists of three main sections which will be solved simultaneously. These are (i) determination of the band edge within the structure, (ii) determination of the absorption at each position in the structure, and (iii) determination of the photoemission and transport of the carriers through the structure. The model will determine the steady-state conditions of the device, considering carriers in the conduction (electron) and valence (light hole, heavy hole, and split-off hole) bands. However, it can be modified to include transients in the detectors as long as the transients are on a time scale that is slow compared to the time for a carrier to transit through the structure.

The quantities that will be calculated at each point are the conduction band edge Φ_c; the cold carrier densities n_{ce}, n_{cl}, n_{ch}, and n_{cs} for the electrons, light, heavy, and split-off holes, respectively; the hot carrier densities $n_{he}(v_\parallel, v_\perp)$, $n_{hl}(v_\parallel, v_\perp)$, $n_{hh}(v_\parallel, v_\perp)$, and $n_{hs}(v_\parallel, v_\perp)$, where $v_\parallel$ and $v_\perp$ are the components of the velocity parallel and perpendicular to the layers, respectively; and the fraction of impurities ionized in the barriers f_i. In addition, the total net charge for the cold carriers and the Fermi level are calculated for each emitter layer.

The device structure, as seen in Fig. 1, consists of a stack of layers of different materials having large enough layer areas so that it can be treated as infinite. This effectively makes the calculation one-dimensional, with the differential equations only depending on the direction perpendicular to the layers. The carriers have a velocity component parallel to the layers, but, as this is constant between collisions, it is easily included as an additional parameter for each carrier that is changed during the collisions. Throughout the discussion, the doped conducting layers are referred to as emitters, with the two outermost emitters also serving as part of the

contacts. The layers with only a residual doping will be referred to as barriers. The individual layers are further divided into smaller sublayers, and all the quantities such as carrier and doping densities, band edges, etc., are calculated and stored for the intersections of the sublayers. At the intersection of an emitter and a barrier, the values are obtained separately for each layer. This allowed the model to easily handle quantities such as the doping and band edges that are discontinuous at the interface between emitters and barriers. For ease of calculation, all the sublayers within a given layer (i.e., in a specific emitter or barrier) were chosen to have the same thickness, although the sublayers of the barriers were larger than for the emitters due to the relatively low net charge density in the barriers compared to the emitters. To perform the calculation, the differential equations were converted into finite difference equations using five point expressions for the derivatives, so the equations at the emitter/barrier interfaces can be evaluated using only points in the emitter or the barrier as desired. This approach allows accurate treatment of quantities that are discontinuous at the emitter/barrier interfaces. The finite difference approach has the advantage of allowing a rapid solution through the use of matrix methods. This makes relaxing the difference equations to the exact solution much faster than using only a shooting method,[14] which is very slow for the stiff equations in the model. The derivatives at the interface between layers will be calculated separately for each layer and will be required to satisfy the appropriate continuity equation.

A. Conduction band edge

The conduction band edge is calculated by solving the Poisson equation with a known space charge in the device,

$$\nabla^2 \Phi_c = \frac{e}{\epsilon_s \epsilon_0}(n_{ce} - n_{cl} - n_{ch} - n_{cs} + n_{he} - n_{hl} - n_{hh} - n_{hs} - f_i n_i), \tag{1}$$

where n_i is the impurity density, f_i is the fraction of impurities ionized, ϵ_s is the static dielectric constant, ϵ_0 is the permittivity of free space, and the hot carrier densities n_{he}, n_{hl}, n_{hh}, and n_{hs} have been obtained by summing over all possible velocities, i.e.,

$$n_{hk} = \sum_{v_\parallel, v_\perp} n_{hk}(v_\parallel, v_\perp), \tag{2}$$

where $k = e, l, h, s$ indicates the band. The main component of the space charge comes from the excess or deficit of cold carriers in the emitter layers and ionized impurities in the barriers, with only small contributions from the hot carriers unless the electric field in a given region is small. The calculation starts with an initial trial band shape, and several iterations are performed until the field is consistent. During this process, the charge in the top and bottom emitters (contacts) is adjusted to match the field at each end of the barrier. With a proper choice of the initial (trial) band edge, this process typically takes only 10–20 iterations.

The first step in obtaining the trial band edge is to obtain a Runge–Kutta method[14] solution of the Poisson equation with only the cold carriers and the impurities considered,

$$\nabla^2 \Phi = \frac{e}{\epsilon}(n_c - f n_i), \tag{3}$$

where $n_c = n_{ce} - n_{cl} - n_{ch} - n_{cs}$ is the total cold carrier density. The initial conditions are $\Phi(0) = 0$ and $\partial\Phi/\partial x$ is a small negative value, typically taken as $\sim 10^{-4}$ times the expected average field in the device, which was found to be sufficiently accurate for the trial function. The trial shape obtained in this calculation does not have to give an exact match to the boundary conditions, only close enough that the relaxation procedure will not oscillate. The cold carrier distribution is assumed to be a Fermi distribution, with the Fermi level chosen so that at the initial point $n_c = n_i$. The results are stored for constant intervals and interpolated to obtain the desired points. This initial process is done for both the positive and negative x directions.

The trial band edge shape is then obtained from the following procedure. In the following discussion, the emitters and barriers are numbered separately, starting from zero at the top and ending at $n-1$ for the barriers and n for the emitters (i.e., there are n barriers and $n+1$ emitters in the structure, as shown in Fig. 1). The change in the slope ΔE_i is calculated from the expected net charge for each emitter, except for the two outer emitters (i.e., for $1 \leq i \leq n-1$). The electric field in each barrier is then calculated using

$$E_i = -\left[\frac{V + \sum_{k=1}^{n-1}(w_k \sum_{j=1}^{k} \Delta E_j)}{\sum_{k=1}^{n-1} w_k} - \sum_{j=1}^{i} \Delta E_j \right], \tag{4}$$

where V is the applied bias and w_k is the thickness of the kth barrier. The equation makes the assumption that the potential difference between the ends of an emitter can be neglected while determining the fields in the barriers. While not sufficiently accurate for a final solution, this approximation is sufficient for the trial solution. The emitter shape is now determined by using the stored data to determine the thickness of the charged layers required to match the fields at the edges of the emitters, and then interpolating from the stored data to determine the shape. For thick emitters (thicker than required to match the slope at the emitter/barrier interfaces), the central region of the emitter is assumed to be at constant potential. For thin emitters, the slopes are fixed at the two ends and the potential is matched in the middle. The center of the internal emitters ($j = 1, \ldots, n-1$) is placed at $V_i = V + \sum_{j=0}^{i}(E_j w_j)$. The outer edge of the top layer is placed at V, and the outer edge of the bottom layer is placed at 0. The barrier shape is found by using straight lines to connect the ends of the emitters with the appropriate offsets for the material differences. While this approach does slightly overestimate the concentration of space charge towards the edges of the emitters, it gives a reasonable starting point that converges quickly. This process only needs to be carried out for the first step of a calculation. After that, the band edge of the previous step can be used as the trial for the next step.

B. Dielectric function for calculating the absorption

The absorption is calculated using the complex dielectric constant. Three different contributions to the absorption are considered: (i) intraband free carrier absorption, (ii) inter-

TABLE I. The values for the parameters used for the intraband portion of the dielectric function for GaN and AlN.

Material	ϵ_s	ϵ_∞	ω_0 (s^{-1})	ω_{TO} (s^{-1})	γ (s^{-1})
GaN	8.9	5.35	6.5×10^{13}	1.31×10^{14}	4.3×10^{12}
AlN	9.14	4.84	6.5×10^{13}	1.4×10^{14}	4.3×10^{12}

band absorption, and (iii) impurity absorption. As the intraband and interband absorptions involve different spectral regions, they are calculated separately and the dielectric function is then merged in the region where the absorption is small for both cases, and the absorption contribution from the impurities in the barrier is then included.

1. Intraband contribution to the absorption

The calculation of the intraband absorption uses the same equation for any material, with the parameters adjusted for the appropriate material. The dielectric function[15] using the two phonon model[16] for the ternary compounds is given by

$$\epsilon(\omega) = \epsilon_\infty \left[1 - \frac{\omega_p^2}{\omega(\omega + i\omega_0)} \right] + \sum \frac{S_j \omega_{TO}^2}{\omega_{TO}^2 - \omega^2 - i\omega\gamma}, \tag{5}$$

where ω_0 is the free carrier damping constant, $\omega_p = \sqrt{Ne^2/\epsilon_0 \epsilon_s m^*}$ is the plasma frequency, ω_{TO} is the TO phonon frequency, γ is the phonon damping coefficient, and $S_j = x(\epsilon_x - \epsilon_\infty)$ is the phonon oscillator strength, with ϵ_s and ϵ_∞ the static and high frequency dielectric functions, respectively, and x the fraction of Ga or Al as appropriate. The sum is over the Ga-like and Al-like phonons for the ternary compounds.

The parameters used for the different materials are given in Table I. The values of the dielectric constants for the alloys were determined by a linear interpolation between the two materials alloyed.

2. Interband contribution to the absorption

The interband absorption for the materials considered was obtained using the model dielectric function (MDF) of Adachi.[16] This approach involves summing the contributions from the one-electron and exciton transitions at the major critical points. A similar approach can be used for other materials although, due to the differences in the crystal structure, the details, such as how many critical points are needed and what directions they lie along, will be different.

For GaN, the approach of Djurisic and Li[17] is used to calculate the interband interactions. This approach is a modification of the MDF of Adachi[18] by including one-electron contributions at the critical points, summing over exciton states other than the ground state, and including frequency dependent damping. The dielectric function in the high energy range is written in the form

$$\epsilon(E) = \epsilon_0(E) + \epsilon_{0E}(E) + \epsilon_1(E) + \epsilon_{1E}(E) + \epsilon_f, \tag{6}$$

where ϵ_0 and ϵ_1 are the one-electron contributions from the E_0 and the E_{1A}, E_{1B}, and E_{1C} critical points, respectively, ϵ_{0E}

and ϵ_{1E} are the exciton contributions at the same critical points; and ϵ_f is the value at infinite energy. The one-electron contribution at the three-dimensional (3D) critical point E_0 is given by

$$\epsilon_0 = A E_0^{-3/2} \chi_0^{-2} [2 - (1 + \chi_0)^{1/2} - (1 - \chi_0)^{1/2}], \qquad (7)$$

where

$$\chi_0 = \frac{E + i\Gamma_0}{E_0}, \qquad (8)$$

with A the strength and Γ_0 the damping constant of the E_0 transition. The exciton contribution at the same point is

$$\epsilon_{0E}(E) = \sum_{m=1}^{\infty} \frac{A_0^{ex}}{m^3} \frac{1}{E_0 - (G_0^{3D}/m^2) - E - i\Gamma_0}, \qquad (9)$$

where A_0^{ex} is the 3D exciton strength parameter and G_0^{3D} is the 3D exciton energy.

The one-electron and exciton contributions at the two-dimensional (2D) E_{1A}, E_{1B}, and E_{1C} critical points are

$$\epsilon_1(E) = - \sum_{\beta=A,B,C} B_{1\beta} \chi_{1\beta}^{-2} \ln(1 - \chi_{1\beta}^2) \qquad (10)$$

and

$$\epsilon_{1E}(E) = \sum_{\beta=A,B,C} \sum_{m=1}^{\infty} \frac{B_{1\beta}^X}{(2m-1)^3} \frac{1}{E_{1\beta} - (G_{1\beta}^{2D}/m^2) - E - i\Gamma_{1\beta}}, \qquad (11)$$

where

$$\chi_{1\beta} = \frac{E + i\Gamma_{1\beta}}{E_{1\beta}}, \qquad (12)$$

with $B_{1\beta}$ and $B_{1\beta}^X$ the corresponding strengths, $\Gamma_{1\beta}$ the damping constant, and $G_{1\beta}^{2D}$ the 2D exciton energy.

The energy dependence of the damping constant is included by writing the damping constants as

$$\Gamma_j'(E) = \Gamma_j \exp\left[- \alpha_j \left(\frac{E - E_j}{\Gamma_j} \right)^2 \right], \qquad (13)$$

where α_j and Γ_j are parameters for the broadening obtained by fitting the measured dielectric constant, and $j = 0, 1A, 1B, 1C$ for the corresponding critical points. The values for the parameters in this model were taken from Ref. 17 and are given in Table II.

The one-electron contribution from the E_1 critical point (along the [111] direction) is

$$\epsilon(E) = - B_1 \chi_1^{-2} \ln(1 - \chi_1^2) - B_{1s} \chi_{1s}^{-2} \ln(1 - \chi_{1s}^2), \qquad (14)$$

with

$$\chi_1 = \frac{E + i\Gamma}{E_1}, \qquad (15)$$

TABLE II. Model parameter values of the GaN interband MDF (Ref. 17).

E_0	3.550 eV
A	41.251 eV$^{3/2}$
Γ_0	0.287 eV
α_0	1.241
A_0^{ex}	0.249 eV
G_0^{3D}	0.030 eV
E_{1A}	6.010 eV
E_{1B}	8.182 eV
E_{1C}	8.761 eV
B_{1A}	0.778 eV
B_{1B}	0.103 eV
B_{1C}	0.920 eV
B_{1A}^x	2.042 eV
B_{1B}^x	1.024 eV
B_{1C}^x	1.997 eV
Γ_{1A}	0.743 eV
Γ_{1B}	0.428 eV
Γ_{1C}	0.440 eV
α_{1A}	0.240
α_{1B}	0.011
α_{1C}	0.005
G_{1A}^{2D}	0.0003 eV
G_{1B}^{2D}	0.356 eV
G_{1A}^{2D}	1.962 eV
ϵ_f	0.426

$$\chi_{1s} = \frac{E + i\Gamma}{E_1 + \Delta_1}, \qquad (16)$$

where B and Γ are the strength and broadening parameters, respectively, of the transitions. The corresponding exciton contribution is

$$\epsilon(E) = \sum_{n=1}^{\infty} \frac{1}{(2h-1)^3} \left(\frac{B_{1x}}{E_1 - [G_1/(2n-1)^2] - E - i\Gamma} \right.$$

$$\left. + \frac{B_2 x}{E_1 + \Delta_1 - [G_{1s}/(2n-1)^2] - E - i\Gamma} \right). \qquad (17)$$

The resulting values are then added together to obtain the complete dielectric function in the interband region.

3. Impurity contributions for the absorption

The impurity contribution to the dielectric function was taken as

$$\epsilon(E) = (1 - f_i) A_i \frac{E_0^2}{E_0^2 - E^2 - iE\Gamma}, \qquad (18)$$

where A_i is the line strength, E_0 is the impurity ionization energy, and Γ is the broadening factor. The factor $1 - f_i$ is the fraction of un-ionized impurities. The impurities contributing to the absorption are selected based on observed features in the spectra of a detector, such as the lines seen at ~ 11 and 13 μm as increased response in Fig. 3, and the line strength which is proportional to the impurity density is adjusted to obtain the best fit to the response. If the impurity density is measured independently, the value of A_i can be calculated.

C. Absorption calculation for intraband and interband transitions

The light propagation through a multilayer structure can be described by the matrix method.[19] There are two waves with electric field amplitudes E^+ and E^- propagating from the top and bottom of each layer, respectively, as shown in Fig. 1. The boundary condition for electric and magnetic fields on the surface between two layers with complex refractive indices n_{j-1} and n_j leads to the matrix T_j describing light penetration from the $(j-1)$th layer to the jth layer as follows:

$$\begin{pmatrix} E_j^+ \\ E_j^- \end{pmatrix} = \frac{1}{2}\begin{pmatrix} 1 + n_{j-1}/n_j & 1 - n_{j-1}/n_j \\ 1 - n_{j-1}/n_j & 1 + n_{j-1}/n_j \end{pmatrix} \cdot \begin{pmatrix} E_{j-1}^+ \\ E_{j-1}^- \end{pmatrix}$$

$$= T_j \cdot \begin{pmatrix} E_{j-1}^+ \\ E_{j-1}^- \end{pmatrix}. \quad (19)$$

Light propagation in the jth layer with thickness d_j is described by the following matrix:

$$D_j = \begin{pmatrix} \exp[i2\pi k(\omega)n_j d_j] & 0 \\ 0 & \exp[-i2\pi k(\omega)n_j d_j] \end{pmatrix}. \quad (20)$$

Here $k(\omega) = \omega/2\pi c$ is the wavenumber, with c the speed of light in vacuum. By requiring only a positively traveling wave at the bottom interface of the structure, the optical electric field strength can be calculated in each of the sublayers. This approach has been used in previous work to calculate the transmission and reflection of arsenide,[15] nitride,[20,21] and antimonide[22] materials, giving good agreement with experimental results.

The photon absorption probability η_a is defined as the fraction of the incident photon flux that is absorbed in the sublayer and is calculated from the following expression:

$$\eta_a = 2\frac{\omega}{c} \, \text{Im}[\epsilon(\omega)]\frac{1}{|E_0|^2}\int_0^W |E(z)|^2 dz$$

$$= 2\frac{\omega}{c} \, \text{Im}[\epsilon(\omega)]\frac{\overline{|E|^2}}{|E_0|^2}W, \quad (21)$$

where $\text{Im}[\varepsilon(\omega)]$ is the imaginary part of the dielectric function, ω is the wave frequency, $\omega/c = 2\pi/\lambda$ is the wave vector of the incident radiation, E is the electric field of the electromagnetic wave inside the layer, E_0 is the electric field of the incident radiation, and W is the thickness of the sublayer.

D. Carrier injection and transport

The final part of the model is the calculation of the injection and transport of the carriers. The injection uses an escape cone approach with all carriers at the interface having sufficient energy to pass over the workfunction entering the barrier. Transport is done by tracking injected carriers as they move through the device, with the various scattering and recombination processes included.

1. Carrier injection into the detector structure

The carrier injection of nonphotoexcited carriers from the emitters was calculated by assuming a Fermi distribution of the cold carriers incident on the emitter/barrier interfaces.

TABLE III. The material and fitting parameters used in calculating the scattering rates. m is the free electron mass.

m_e	$0.2m$
m_l	$0.3m$
m_h	$1.4m$
m_{so}	$0.6m$
DK	4×10^{21} eV^2/m^2
A_i	1.5×10^{-15} m^2
B_i	5.3×10^{-16} m^2

The transmission probability for the carriers past the barrier, either by thermionic emission over the barrier or tunneling through the barrier, was calculated using the method of Gundlach,[23] which has been corrected for the mass difference in the layers as follows:

$$T = \frac{4k_3}{\pi^2 k_1}\left(\left\{[\text{Ai}(z_0)\text{Bi}'(z_b) - \text{Bi}(z_0)\text{Ai}'(z_b)]\right.\right.$$
$$+ \frac{k_3}{k_1}[\text{Bi}'(z_0)\text{Ai}(z_b) - \text{Ai}'(z_0)\text{Bi}(z_b)]\bigg\}^2$$
$$+ \left\{\frac{m_e}{k_1 l m_b}[\text{Ai}'(z_0)\text{Bi}'(z_b) - \text{Bi}'(z_0)\text{Ai}'(z_b)]\right.$$
$$\left.\left.+ \frac{k_3 l m_b}{m_e}[\text{Ai}(z_0)\text{Bi}(z_b) - \text{Bi}(z_0)\text{Ai}(z_b)]\right\}^2\right)^{-1}, \quad (22)$$

where $z_0 = \lambda$, $z_b = \lambda - b/l$, $l = (\hbar^2 b/2m_b e\Delta V)^{1/3}$, $\lambda = (2m_b/\hbar^2) \times (\Delta E - E_x)l^2$, $k_1 = \sqrt{2m_e E_x}/\hbar$, $k_3 = \sqrt{2m_e(E_x + e\Delta E)}/\hbar$, m_e is the effective mass in the emitter, m_b is the effective mass in the barrier, b is the barrier width, ΔV is the bias, ΔE is the barrier height, E_x is the electron energy associated with motion perpendicular to the layers, and Ai and Bi are the Airy functions with their derivatives Ai$'$ and Bi$'$.

The rate of injected carriers is found from

$$\sigma(v,v_\perp) = v_\perp n(v)T(v_\perp). \quad (23)$$

The carriers passing the emitter/barrier interface are then added to the appropriate hot carrier density in the barrier.

E. Scattering mechanisms for the transport

In order to determine the transport of the carriers, the rates need to be determined for the various scattering processes (ionized impurity, polar optical, and nonpolar optical). These were calculated following Brudevoll et al.[24] and references therein. The material parameters for the scattering calculations are given in Table III. Throughout the remainder of this section, i and f will refer to the initial and final values of a quantity, respectively.

1. Ionized impurity scattering

The ionized impurity scattering rate (P^{im}) was taken as

$$P_{if}^{\text{im}} = \frac{3e^4 n_I f_I m_f F}{32\pi\hbar^3\epsilon_0\epsilon_s k_i^2 k_f}, \quad (24)$$

where for intraband scatterings

$$F^{\text{intra}} = \frac{\beta^2 + 2k^2}{k^2} \ln\left(\frac{\beta^2}{\beta^2 + 4k^2}\right) + \frac{4}{3}\left(\frac{3\beta^4 + 12\beta^2 k^2 + 8k^4}{\beta^2(\beta^2 + 4k^2)}\right) \tag{25}$$

and for interband scatterings

$$F^{\text{inter}} = \frac{\beta^2 + k_i^2 + k_f^2}{k_i k_f} \ln\left(\frac{\beta^2 + (k_i + k_f)^2}{\beta^2 + (k_i - k_f)^2}\right) - 4, \tag{26}$$

where

$$\beta = \left(\frac{n_I f_I e^2}{k_B T \epsilon_0 \epsilon_s}\right)^{1/2}. \tag{27}$$

Here n_I and f_I are the impurity density and the fraction of impurities ionized, respectively, m_i and m_f are the initial and final state masses, respectively, and the initial and final state wave vectors are related by

$$k_f^2 = k_i^2 m_f / m_i. \tag{28}$$

2. Polar optical phonon scattering

The polar optical phonon scattering rate (P^{po}) was taken as

$$P_{if}^{\text{po}} = \frac{e^2 \omega_0 m_f}{4\pi\epsilon_0 \hbar^2}\left(\frac{1}{\epsilon_\infty} - \frac{1}{\epsilon_s}\right)\left\{\begin{matrix} N_0 \\ N_0 + 1 \end{matrix}\right\}\frac{\Psi H}{k_i}, \tag{29}$$

where N_0 is used for absorption and $N_0 + 1$ for emission, $\Psi = \ln|(k_i + k_f)/(k_i - k_f)|$, and for the intraband and interband processes

$$H^{\text{intra}} = [1 + 3\Phi(\Phi - \Psi^{-1})/4 , \tag{30}$$

$$H^{\text{inter}} = 3[1 - \Phi(\Phi - \Psi^{-1})/4 , \tag{31}$$

with $\Phi = (k_i^2 + k_f^2)/(2k_i k_f)$

3. Nonpolar optical phonon scattering

The nonpolar optical phonon scattering rate (P^{npo}) is

$$P_{ij}^{\text{npo}} = \frac{(DK)^2 m_f^{3/2}}{2\sqrt{2}\pi\hbar^3 \omega_o}(E \pm \hbar\omega_0)^{1/2}\left\{\begin{matrix} N_0 \\ N_0 + 1 \end{matrix}\right\}, \tag{32}$$

where $(DK)^2 = 4(\omega_0/s_l)^2 E_l^2$ is the optical phonon coupling constant and ρ is the density of the material.

4. Impact ionization and recombination

The impact ionization and recombination rates of the impurities/defects in the barrier were treated as parameters that were determined from fitting the dark current. For both of these rates, the simplifying assumption that they do not depend on the hot carrier energy was made. As the impacting carriers should have sufficient energy to overcome the binding energy of the impurity, impact ionization should have a threshold limit. The rates for ionization (P^{ii}) and capture (P^{ic}) were taken to be of the form

$$P^{ii} = A_i v(1 - f_i)n_i \tag{33}$$

for impact ionization and

$$P^{ic} = B_i v f_i n_i \tag{34}$$

for recombination, where the constants A_i and B_i were the cross sections for impact ionization and capture, respectively.

F. Calculation of the hot carrier transport

The dark current transport was determined by injecting carriers randomly selected from the hot carrier distribution in the injection contact. Each injected carrier was then tracked as it moved through the device structure until it either reached one of the contacts, was captured by an emitter or impurity ion, or was involved in an electron-hole recombination. The position and velocity of the carriers were recorded at regular time intervals δt and used to calculate a steady-state distribution function for the hot carriers. To smooth out the distribution, the initial injection time for the carriers was randomly chosen in the range from 0 to δt. To follow the path of the hot carrier, the probability of a scattering event was calculated by considering small time steps ($t \ll 1/P$ for all processes) so that the probability of multiple scatterings in a given time step was negligible. If there was no scattering, the new position and velocity of the carrier at the end of the time step were determined. If scattering occurred, the carrier was transported to the scattering location, and a new velocity is calculated based on the scattering process. For ionized impurity and optical phonon scattering, the final velocity direction is chosen randomly. For impact ionization, the carriers are assumed to conserve energy and momentum, and the direction of their motion in the center of mass frame is determined randomly. This process is repeated until one of the following three events occurs: (i) the carrier exits the device by entering one of the last emitters, (ii) the carrier is captured at an impurity, or (iii) the carrier reaches an emitter/barrier interface with an energy less than that of the barrier, in which case it is assumed to be captured by the emitter. For each injection case, a large ($10^4 - 10^5$) number of carriers are randomly chosen and used to produce a current density. The current densities are then multiplied by the total number of carriers injected at that location and summed to obtain the total carrier density. The current density at each location is then calculated from the total current density by

$$j(x) = e \sum N(v, v_\perp)v_\perp. \tag{35}$$

The hot carrier generation and capture are checked for each emitter and for each point in the barrier to ensure that they are negligibly small. If that is true, the current density calculated is the desired current. Otherwise, the impurity ionization and net charge in the emitters are adjusted and the process repeated.

III. PERFORMANCE COMPARISON WITH EXPERIMENTAL RESULTS

The primary goal of this work was to develop a model that could describe both the UV and IR responses[25] of GaN/AlGaN detectors in order to design optimized dualband detectors. Once the model has been developed and tested on GaN detectors, it can be readily extended to other detectors such as GaAs.[12] Hence the model was first compared with
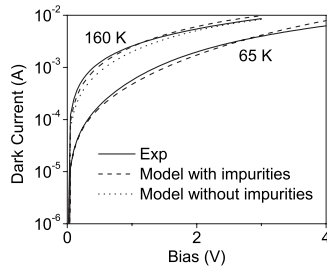
FIG. 2. The dark current fit for the GaN device at 65 and 160 K. The GaN detector required a high impurity density and a large fraction of ionized impurities in the barrier to obtain a good fit. Also shown is the curve obtained at 160 K without impurities showing the poorer fit at low bias.

FIG. 3. Measured and calculated responses for the GaN sample. UV response at 300 K and a −0.5 V bias, and response at −1.0 V and 5.3 K. Note that although the response is only shown in the two ranges of interest, the model calculates the response over the entire range from the UV to the IR.

the experimental results for a n-GaN/AlGaN detector with 5×10^{18} cm^{-3} doped GaN emitters and a 0.6 μm Al$_{0.026}$Ga$_{0.974}$N barrier that has shown both UV and IR responses.[25] During the fitting process, the only parameter that was adjusted was the impurity density.

A. Dark current comparison

The dark current was used to determine the impurity density in the barrier by fitting the current at different temperatures. The ionization and recombination rates were assumed to be independent of the temperature, which was sufficiently accurate for the present data. Only the thermal or tunneling injection of the cold carriers in the emitters was included for this part of the calculation. The results for the dark current comparison are shown in Fig. 2. The n-GaN detector results[25] show good agreement between the experiment and the model. To match the experimental dark current, it was necessary to include a large impurity density ($\sim 10^{17}$ cm^{-3}), with nearly all of the impurities near the injection contact being ionized at higher bias. If these ionized impurities are not considered, the dark current was too low at low bias, as shown in Fig. 2.

The need for impurities can be understood by considering the results for the band shape before and after iteration for the band edge of a single barrier detector. The band bending in the barrier is due to the impurities which are almost totally ionized by impact ionization. Only in regions were the field is near zero will the capture rate be sufficiently high to maintain a significant fraction of un-ionized impurities. At low impurity densities, there is a single field region for the barrier in which the impurities are almost totally ionized, and the field continually decreases from a maximum at the injection contact to a minimum at the collection contact. However, for higher impurity densities (or thicker barriers), the field will eventually decrease to nearly zero. At that location, capture will start to dominate ionization and the impurities will be almost totally un-ionized. Throughout this second region, the field should be nearly zero. The relationship between the critical impurity density, barrier thickness, and bias voltage can be obtained by assuming that the impurities are totally ionized and that the field at the collector contact has just reached zero and is given by

$$\Delta V = \frac{e n_i w^2}{2 \epsilon_0 \epsilon_s},\tag{36}$$

where ΔV is the applied voltage bias, ϵ_s is the static dielectric constant for the barrier, and w is the barrier thickness. If ΔV is below the value given by Eq. (36), the detector will have the maximum effect from impurities, while for biases above the critical value, the effects of the impurities will be decreased.

The field at the injection contact will decrease as the barrier width is increased up to the critical thickness, and then remain nearly constant. Hence, the dark current for a fixed voltage bias will also decrease with barrier thickness up to the critical thickness, and then remain relatively constant.

B. Responsivity comparison with the experiment

The responsivity of the detector was calculated using a known power density (~ 1 μW/cm^2) of radiation incident on the detector. The current is then calculated as before, using both the injection and the photoexcitation contributions. The difference between the current calculated in this step and the dark current calculated previously is the photo (response) current. Experimental and model spectral response comparisons for the GaN detector are shown in Fig. 3. The UV response shows a reasonable agreement in the line shape although the overall model response is lower than the experimental response and does not show the small variations observed for the experimental data. The peak responsivity of 0.55 mA/W corresponds to noise equivalent power (NEP) of 1×10^{-8} W at room temperature. At the background limited infrared photodetection (BLIP) temperature of 41 K, the NEP would be decreased to 5×10^{-11} W. When the UV detection is optimized to reach typical maximum values of ~ 100 mA/W, the NEP would be $\sim 10^{-12}$ W, which would be comparable with standard commercial detectors.

The strength and broadening of the impurity lines in the IR region were determined from fitting the data, while the line locations were taken from previously known values for observed impurity transitions.[26] The results for the IR region show very good agreement with the observed spectra. The small variations observed near 9 μm are probably due to an additional unidentified impurity response that is not included in the model.

These results show that the model explains the response in both the UV and IR regions of the detector. The same model can also be used on other direct gap materials. For example, by changing the material parameters results could also be obtained for GaAs detectors. For an optimized detector using 1×10^{19} cm^{-3} doped emitters and a 1.2 μm thick Al$_{0.026}$Ga$_{0.974}$N barrier with an impurity density of 1×10^{15} cm^{-3}, the responsivity should be ~5 A/W at 10 μm. The calculated photoresponse for this detector is shown in Fig. 9. The maximum quantum efficiency of the detector is 65% for free carrier response at 10 μm, and with the impurity contribution at 12 μm, it is increased to 80%. The efficiency could be further increased by increasing the impurity density; however, this would also lead to increased tunneling currents which are not in the model. These would decrease the responsivity. The chosen value is a conservative limit for which this is not expected to occur. However, the value given is very close to the maximum possible value for a single layer detector. Further improvements would require multiple layers.

C. Calculation of the specific detectivity *D*∗

The determination of $D*$ requires that the noise be determined. It will be assumed that the primary noise component is shot noise, given by

$$S_i = 2qI_d g, \tag{37}$$

where q is the electron charge, I_d is the dark current, and g is the gain factor, with the same gain factor as the IR photocurrent which corresponds to the dominant current component. The responsivity calculations for the IR detector being used as a comparison gave an IR photocurrent gain of 3.3. The detectivity $D*$ can then be calculated from

$$D* = R_p A^{1/2} / S_i^{1/2} \text{ Jones}. \tag{38}$$

By using the results obtained from the responsivity and dark current calculations, $D*$ was calculated to be 9.3 $\times 10^9$ Jones at 12 μm and 5.3 K for the IR detection, and 3.7×10^7 Jones for the UV detection at 360 nm for a detector temperature of 300 K.

IV. EFFECTS OF VARYING DEVICE PARAMETERS

In order to optimize the device performance, the effects of varying the device parameters were studied. Here the concentration will be on variations which can affect the gain in the device as the effects involving response range selection are generally understood and will not produce significant changes in the responsivity. The parameters producing a change in the gain are the barrier thickness, the impurity density in the barrier, and the recombination rate for the electron-hole pairs.

For the IR response, the gain mechanism comes primarily from the balance of carrier capture by ionized impurities and impact ionization of neutral impurities. As both these rates will depend on the density of impurities, that dependence would be expected. However, the barrier thickness also affects the gain by changing the bias field distribution in the barrier. For thinner barriers, the field tends to be more
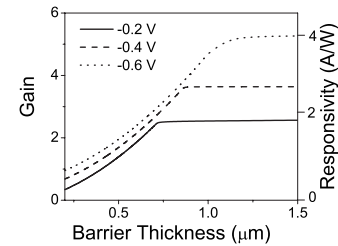
FIG. 4. The calculated IR gain and responsivity for a single barrier detector at three different biases as the barrier width is varied. The emitter doping was 5×10^{18} cm^{-3} and the impurity density in the barrier was 1×10^{17} cm^{-3}.

uniform, and the gain factor is nearly 1. As the barrier becomes thicker, it develops a highly ionized region near the injection contact, producing a high field, while the region near the collector contact is primarily neutral and has a low field. Under these conditions there are more ionizations and captures leading to a higher gain factor. The effects of varying barrier thickness at several different biases for an impurity density of 10^{17} cm^{-3} are shown in Fig. 4. The effects of varying the impurity density in the barrier on the gain are shown in Fig. 5, where larger gains are observed for higher barrier doping densities. Increasing the doping in the emitters did not produce any significant changes in the gain.

The UV gain is affected primarily by the electron-hole recombination rate as the barrier will typically be thick enough for total absorption of the UV radiation. This rate is related to the density of scattering centers for the holes in the barrier. The defects involved in the recombination for this specific detector structure have not been definitely identified, but one possibility is Ga vacancies, which form a deep hole trap with charge $-3e$. This trap has a hole capture cross section of 10^{-14} cm^{-2}, and after the hole is captured, the cross section for electron capture is 10^{-21} cm^{-2}. The capture of a hole followed by an electron will serve as the recombination mechanism. The presence of Ga vacancies is indicated by the observed yellow band in photoluminescense measurements of the detector sample. Under illumination, the traps are found to almost entirely have captured holes so the recombination rate is limited by the electron rate. As the electron density is almost constant, the recombination will be nearly linear in the trap density. For the detector whose response was fitted as in Fig. 3, the trap density would be 3.4×10^{16} cm^{-3}. This density determination neglects the possibility of other traps with different charge states and hence faster electron capture. The Ga vacancy is negatively charged
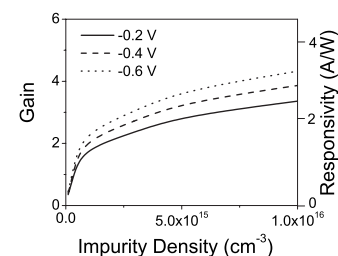
FIG. 5. The calculated IR gain and responsivity for a single barrier detector at three different biases as the impurity density in the barrier is varied. The emitter doping was 5×10^{18} cm^{-3} and the barrier width was 0.6 μm.
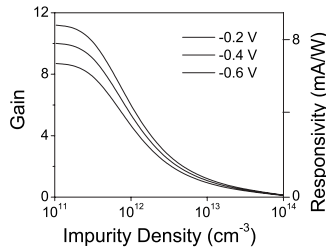
FIG. 6. The calculated UV gain and responsivity for a single barrier detector at three different biases as the impurity density in the barrier is varied. The emitter doping was 5×10^{18} cm^{-3} and the impurity density in the 0.6 μm barrier was 1×10^{17} cm^{-3}.
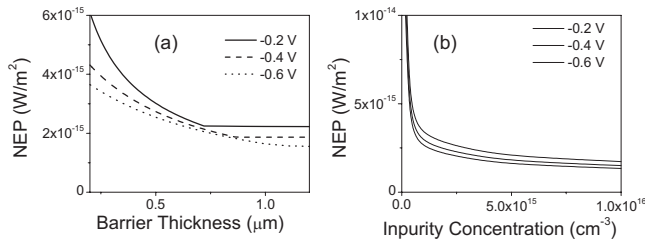
FIG. 7. The calculated variation of the NEP with (a) barrier thickness having an impurity density of 1×10^{17} cm^{-3} and (b) impurity concentration in a 0.6 μm thick barrier.
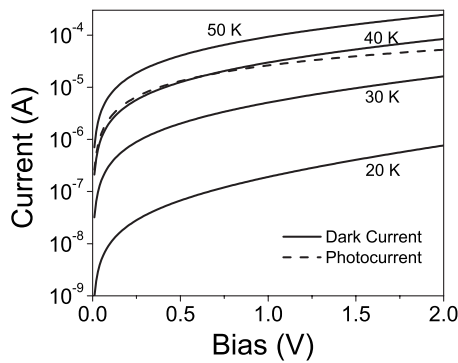
FIG. 8. The calculated dark current at temperatures of 20–50 K and the photocurrent from a 300 K background. The detector was assumed to have an optical area of 260 μm on a side and an electrical area of 400 μm on a side.
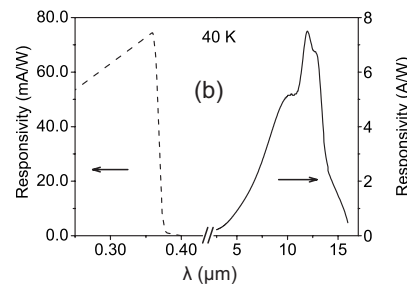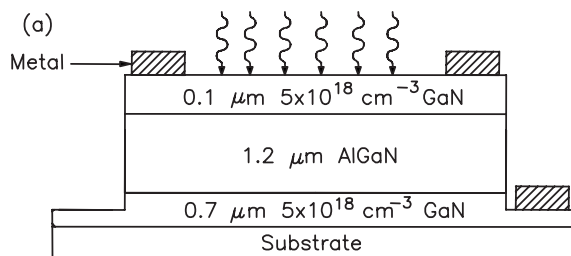
even after the hole has been captured. This reduces the cross section for electron capture. Traps with lower charge states would capture the electrons more efficiently and require a lower trap density to explain the observed results. As the mean free path depends on the velocity of the holes and hence the bias, the response should increase with bias and then saturate at some value. The effects of varying the defect density on the detector performance are shown in Fig. 6.

The variation of the NEP with barrier thickness and impurity concentration is shown in Fig. 7. As the gain increases, the NEP decreases for the detectors. The change is most noticeable for the varying impurity concentration, in which the gain becomes very small at low impurities, leading to a much higher NEP. For the optimized detector described above, the best NEP would be $\sim 1.5 \times 10^{-15}$ W/m^2. By using a 60° conical field of view, the calculated BLIP temperature of all the curves shown was 41 K for a detector with a 15 μm threshold. This temperature does not change significantly with variation of barrier thickness or impurity concentration as the changes in gain affect both the photo and dark currents similarly, causing most of the effects of these parameters to cancel out. The most significant value for the BLIP is the threshold. Plots of the dark current and the 300 K background photocurrent on a detector with 260 μm square optical area and 400 μm square electrical area are shown in Fig. 8

By using the above results, an optimized design for a single barrier detector with a 15 μm threshold was developed. The optimized detector should consist of a 0.1 μm thick, 1×10^{19} cm^{-3} doped GaN top emitter and a 1.2 μm thick Al$_{0.026}$Ga$_{0.974}$N barrier with an impurity density of 1×10^{15} cm^{-3} and a 0.7 μm thick, 1×10^{19} cm^{-3} doped GaN bottom emitter. The responsivity would be ~ 5 A/W at 10 μm and 77 K. The calculated photoresponse for this detector is shown in Fig. 9. The maximum quantum efficiency of the detector is 65% for free carrier response at 10 μm, and with the impurity contribution at 12 μm, it is increased to 80%. The efficiency could be further increased by increasing the impurity density; however, this would also lead to increased tunneling currents which are not in the model. These would decrease the responsivity. The chosen value is a conservative limit for which this is not expected to occur. For the optimized detector described above, the best NEP would be $\sim 1.5 \times 10^{-15}$ W/m^2. By using a 60° conical field of view, the calculated BLIP temperature of all the curves shown was 41 K for a detector with a 15 μm threshold.

FIG. 9. (a) The design for the optimized single layer detector. (b) The calculated photoresponse at 40 K for an optimized detector using 5×10^{18} cm^{-3} doped emitters and a 1.2 μm thick Al$_{0.026}$Ga$_{0.974}$N barrier having an impurity density of 1×10^{15} cm^{-3}.
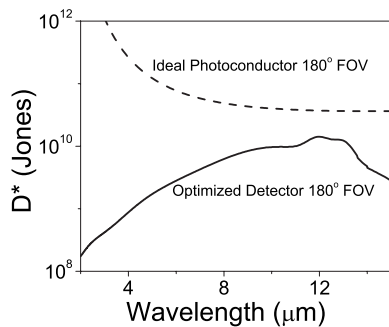
FIG. 10. The calculated D^* for the optimized design and for an ideal photoconductor. The maximum D^* with a 180° field of view was ~35% of the ideal value.

Shown in Fig. 10 is the specific detectivity at 77 K for the optimized detector as well as for an ideal photoconductor with a 180° field of view. The peak D^* was 1.4×10^{10} Jones, which is ~35% of the ideal value. The low value of D^* is due to the low absorption (~40%) in the emitter layer. The doping in the emitter is at the limits for practical applications and so cannot be increased to improve the absorption significantly. While the total absorption can be improved by using multiple emitters, experimental results on other detector have indicated that the gain is then reduced, leaving the total response nearly unchanged. Further work will be carried out to improve the D^* value.

V. CONCLUSIONS

A model describing the spectral response over a wide range covering both interband and intraband transitions is compared with the experimental results for devices with a single barrier. The model agrees well with the GaN/AlGaN detector experimental results covering both the UV and IR regions, and it should be possible to extend to other direct band gap materials. This improved model is based on using the dielectric function to calculate the absorption and using a semiclassical scattering approach to calculate the transport of carriers using the hole and electron bands. This approach has the advantage of allowing calculation of both interband and intraband transitions as well as any impurity contributions. The bias dependence is also obtained directly unlike in the previous models for response in HIWIPs and HEIWIPs. An additional advantage of this approach is that it can be readily extended to include other mechanisms as was done in adding the impurity absorption or in combining the different scattering mechanisms. For an optimized detector using 5×10^{18} cm^{-3} doped emitters and a 1.2 μm thick Al$_{0.026}$Ga$_{0.974}$N barrier with an impurity density of 1×10^{15} cm^{-3}, the responsivity should be ~5 A/W and the NEP ~1.5×10^{-15} W/m^2 at 10 μm and 77 K. Although testing and optimization on multiple emitter structures are still on going, the method should also work for those structures.

Further improvement in the response, operating temperature, material quality, detector design, etc., is needed for use of these detectors in arrays.

[1] J. Li, K. K. Choi, and D. C. Tsui, Appl. Phys. Lett. **86**, 211114 (2005).
[2] E. Dupont, M. Gao, Z. Wasilewski, and H. C. Liu, Appl. Phys. Lett. **78**, 2067 (2001).
[3] S. D. Gunapala, S. V. Bandara, J. K. Liu, S. B. Rafol, and J. M. Mumolo, Proc. SPIE **5234**, 272 (2004).
[4] S. Krishna, D. Forman, S. Annamalai, P. Dowd, P. Varangis, T. Tumolillo, Jr., A. Gray, J. Zilko, K. Sun, M. Liu, J. Campbell, and D. Carothers, Appl. Phys. Lett. **86**, 193501 (2005).
[5] S. Chakrabarti, X. H. Su, P. Bhattacharya, G. Ariyawansa, and A. G. U. Perera, IEEE Photonics Technol. Lett. **17**, 178 (2005).
[6] A. G. U. Perera, H. X. Yuan, and M. H. Francombe, J. Appl. Phys. **77**, 915 (1995).
[7] D. G. Esaev, M. B. M. Rinzan, S. G. Matsik, and A. G. U. Perera, J. Appl. Phys. **96**, 4588 (2004).
[8] V. E. Vickers, Appl. Opt. **10**, 2190 (1971).
[9] J. M. Mooney and J. Silverman, IEEE Trans. Electron Devices **32**, 33 (1985).
[10] M. B. M. Rinzan, A. G. U. Perera, S. G. Matsik, H. C. Liu, Z. R. Wasilewski, and M. Buchanan, Appl. Phys. Lett. **86**, 071112 (2005).
[11] A. G. U. Perera, S. G. Matsik, P. V. V. Jayaweera, K. Tennakone, H. C. Liu, M. Buchanan, G. Von Winckel, A. Stintz, and S. Krishna, Appl. Phys. Lett. **89**, 131118 (2006).
[12] G. Ariyawansa, M. B. M. Rinzan, D. G. Esaev, S. G. Matsik, A. G. U. Perera, H. C. Liu, B. N. Zvonkov, and V. I. Gavrilenko, Appl. Phys. Lett. **86**, 143510 (2005).
[13] S. G. Matsik, M. B. M. Rinzan, A. G. U. Perera, H. C. Liu, Z. R. Wasilewski, and M. Buchanan, Appl. Phys. Lett. **82**, 139 (2003).
[14] W. H. Press, B. P. Flannery, S. A. Teukolsky, and W. T. Vetterling, *Numerical Recipes* (Cambridge University Press, Cambridge, England, 1986).
[15] M. B. M. Rinzan, D. G. Esaev, A. G. U. Perera, S. G. Matsik, G. Von Winckel, A. Stintz, and S. Krishna, Appl. Phys. Lett. **85**, 5236 (2004).
[16] S. Adachi, *GaAs and Related Materials* (World Scientific, Singapore, 1994), p. 439.
[17] A. B. Djurisic and E. H. Li, Appl. Phys. Lett. **73**, 868 (1998).
[18] T. Kawashima, H. Yoshikawa, S. Adachi, S. Fuke, and K. Ohtsuka, J. Appl. Phys. **82**, 3528 (1997).
[19] M. V. Klein and T. E. Furtac, *Optics* (Wiley, New York, 1986).
[20] M. H. Kane, M. Strassburg, W. E. Fenwick, A. Asghar, J. Senawiratne, D. Azamat, Z. Hu, E. Malguth, S. Graham, U. Perera, W. Gehlhoff, A. Hoffmann, N. Dietz, C. J. Summers, and I. T. Ferguson, Phys. Status Solidi C **3**, 2237 (2006).
[21] Z. G. Hu, A. B. Weerasekara, N. Dietz, A. G. U. Perera, M. Strassburg, M. H. Kane, A. Asghar, and I. T. Ferguson, Phys. Rev. B **75**, 205320 (2007).
[22] Z. G. Hu, A. G. U. Perera, Y. Paltiel, A. Raizman, and A. Sher, J. Appl. Phys. **98**, 023511 (2005).
[23] K. H. Gundlach, Solid-State Electron. **9**, 949 (1966).
[24] T. Brudevoll, T. A. Fjeldly, J. Baek, and M. S. Shur, J. Appl. Phys. **67**, 7373 (1990).
[25] G. Ariyawansa, M. B. M. Rinzan, M. Alevli, M. Strassburg, N. Dietz, A. G. U. Perera, S. G. Matsik, A. Asghar, I. T. Ferguson, H. Luo, A. Bezinger, and H. C. Liu, Appl. Phys. Lett. **89**, 091113 (2006).
[26] C. B. Soh, S. J. Chua, H. F. Lim, D. Z. Chi, S. Tripathy, and W. Liu, J. Appl. Phys. **96**, 1341 (2004).